

Implemented Finite Element Routines for the Calculation of Quasi-Steady and Transient Characteristics of a Squirrel Cage Induction Machine

J. Bacher and C. Grabner

Abstract—Successful optimization processes of highly utilized industrial squirrel cage induction machines enforces fast, reliable and accurate design concepts. Therefore, modern numerical finite element calculation procedures, which incorporate moveable rotor parts, non-linear iron saturation effects and realistic geometric properties, have been systematically established and applied to an induction motor in the time-domain for the prediction of several transient and quasi-steady characteristics. The obtained results have been compared with measurements in order to verify the assumptions within the finite element modeling.

Index Terms—Induction machine, transient behavior, quasi-steady characteristics, finite element method.

I. INTRODUCTION

The squirrel cage induction machine is preferably used in low performance industrial fix speed or variable speed applications due to the very high overload capability, reliability as well as robustness which has been proven over several decades. This investigation is based on an industrial low voltage motor, as shown in Fig. 1, with rated output power of 3 kW, rated voltage of 400 V, rated speed of approximately 1420 rpm and rated torque of 20 Nm.

For the design and cost optimization process of such squirrel cage induction machines it is advisable to perform in addition to the well known analytical calculation approach, some results for the considered 3 kW machine are listed in Fig. 2 and Fig. 3, also more sophisticated numerical investigations with combined quasi-steady as well as transient electromagnetic Finite Element techniques [1,2]. This has become feasible due to the rapid and continuous progress in computer science.

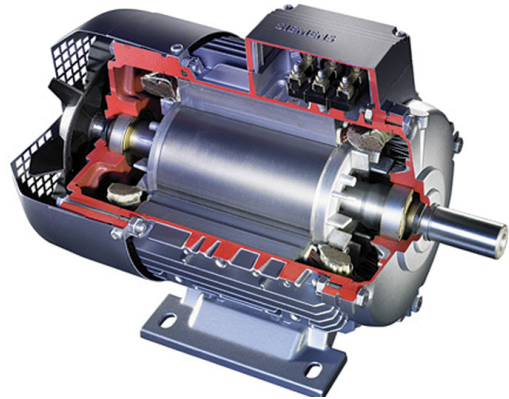


Fig. 1: Typical cross section of a squirrel cage induction motor.

LEISTUNG	3.00	NETZSPG.	400.0	PHASENSPG.	400.0	FOLZZAHL	4	FREQUENZ	50.000	STP.TEMP.	64.5		
ERR.: MA/NN	2.75	IA/IN	6.30	MK/NN	2.95	ETA %	83.00	C-PHI	0.820	STD.TEMP.	67.0		
GER.: MA/NN	2.71	IA/IN	6.11	MK/NN	2.73	ETA %	81.64	C-PHI	0.807	STD.TEMP.	67.0		
DA 1	145.0	TKD11	NTF 6019	BZK 1	3.67	BK 2	15937	L ST	130	BR	13		
DA 2	88.0	TKD21	NTA 6019	BZK 2	4.72	BK 2	15937	L ST	130	BR	13		
DI 1	32.0	TKD22	S	1.0	BZM 2	4.72	BM 2	15953	ON	49.00	HR	18.08	
DI 2	32.0	TKD22	S	1.0	BZM 2	4.72	BM 2	15953	ON	49.00	HR	18.08	
LO 1	130	TKD22	A	1.50	BZF 2	4.73	BF 2	15905	K	23.44	OR	235.04	
LO 2	130	TKD22	B	1.50	LL 2	2.73	EV 2	16939	K	23.44	OR	235.04	
NZ 1	2.28	TKD22	T	1.6	LL 2	2.73	EV 2	16939	K	23.44	OR	235.04	
NZ 2	2.28	TKD22	T	1.6	LL 2	2.73	EV 2	16939	K	23.44	OR	235.04	
TAUN2	9.88	B	1	16.01	HV 2	11.50	HV 2	0	0	0	0		
SCHN:	7.68	B	1	16.01	HV 2	11.50	HV 2	0	0	0	0		
S2FE	1.48	BZK	DJ 2	43.50	DJ 2	43.50	DJ 2	43.50	DJ 2	43.50	DJ 2	43.50	
S3FE	1.48	BZK	DJ 2	43.50	DJ 2	43.50	DJ 2	43.50	DJ 2	43.50	DJ 2	43.50	
S4FE	1.48	BZK	DJ 2	43.50	DJ 2	43.50	DJ 2	43.50	DJ 2	43.50	DJ 2	43.50	
S2EN	1.04	BZK	DJ 2	43.50	DJ 2	43.50	DJ 2	43.50	DJ 2	43.50	DJ 2	43.50	
KCM 1	1.340	XN1	3.5437	XN1 A	3.5145	AWJ 1	89.1	IL	3.717	SB 1	6.339	BL-S	3.6
KCM 2	1.344	XC1	3.5777	XG1 A	3.5777	AWJ 1	89.1	IL	3.717	SB 1	6.339	BL-S	3.6
KCM 3	1.048	XLB1	3.0341	XLA1	7.847	AWJ 1	89.1	IL	3.717	SB 1	6.339	BL-S	3.6
KCM 4	1.051	XBI	3.1555	XBI	3.2668	AWJ 1	89.1	IL	3.717	SB 1	6.339	BL-S	3.6
KCB 1	1.413	XHB	1.6227	VA	4.1000	S	865.2	IH	215.0	SNA 2	13.84	V J	63.2
KCB 2	1.413	XHB	1.6227	VA	4.1000	S	865.2	IH	215.0	SNA 2	13.84	V J	63.2
KCB 3	1.413	XHB	1.6227	VA	4.1000	S	865.2	IH	215.0	SNA 2	13.84	V J	63.2
KCB 4	1.413	XHB	1.6227	VA	4.1000	S	865.2	IH	215.0	SNA 2	13.84	V J	63.2
VB 1	1.6731	3*RXI	15.3007	K S	0.25	STRF	0	0	0	0	0	0	0
VB 2	1.4522	3*RWI	19.2544	R A	2.4483	X LR2	4.5071	X LA2	1.4476	X K	16.252	COG-S	7870
R	51.1664	R ST	1247	R A	2.4483	X LR2	4.5071	X LA2	1.4476	X K	16.252	COG-S	7870
R 1	6.6550	R RG2	0141	R*HR3	6.4319	X OMB	0.0000	X OA	0.0000	X A	10.645	COG-M	8623
S 1	815.10	R B 2	1389	R*HA3	7.1599	X NBS	4.8041	X NA3	4.3020	Z K	20.712	COG-N	7951
S 2	2.6274	R B 2	7.1046	R K	12.8401	X B	5.3112	X A	5.7504	Z A	17.253	COG-N	7951
S 2	863.40	R B 2	7.1046	R K	12.8401	X B	5.3112	X A	5.7504	Z A	17.253	COG-N	7951
M N	20.25	N	1415.3	SIG.M	0.05644	F A	0.7450	X HA2	5.0968	XK/ZN	1.1542	COG-N	7951
M K	55.20	N K	762.2	SIG.K	0.49188	F A	0.7450	X HA2	5.0968	XK/ZN	1.1542	COG-N	7951
M A	54.77	N S	1500.0	SIG.N	0.49188	F A	0.7450	X HA2	5.0968	XK/ZN	1.1542	COG-N	7951
R ST/RG	8.8167	RHA2/RA	0.5273										
R*ST/RHA2	1.0403												

Fig. 2: Various results of the well known analytical quasi-steady calculation approach.

Manuscript received August 13, 2008.
 Johann Bacher is with the Institute of Drive Technology and Electrical Machines, Kopernikusgasse 24, A-8010 Graz, Austria (e-mail: johann.bacher@tugraz.at).

Christian Grabner is with the Research and Development Department for Drive Systems, Siemens AG, Frauenaucherstrasse 80, D-91056 Erlangen, Germany, (e-mail: grabner.christian@siemens.com).

MOMENTENKENNLINIE	FUR DIE POLZAHL=	4	QUERWIDERSTAND=	.10000			
DREHZ.	GR. MOM.	STROM	COS-PHI	MOM. UN	MOM. IS	LFR-STR	A
0	54.77	40.16	.787	68.47	67.84	1696.13	
125.0	56.37	38.91	.796	70.20	70.09	1642.40	
250.0	57.99	37.48	.805	69.50	69.90	1581.24	
375.0	58.26	35.51	.808	68.69	69.90	1497.01	
500.0	61.06	34.05	.828	70.91	72.18	1433.40	
583.3	61.82	32.67	.837	71.00	72.51	1373.93	
666.7	62.33	31.13	.846	70.70	72.42	1307.41	
750.0	62.66	29.45	.857	70.14	71.97	1234.96	
833.3	62.46	27.56	.867	68.92	70.83	1153.05	
916.7	61.72	25.45	.878	67.07	68.95	1061.89	
1000.0	60.11	23.08	.890	64.26	66.02	959.21	
1050.0	58.58	21.52	.896	61.99	63.62	891.29	
1100.0	56.49	19.84	.903	59.15	60.62	817.98	
1150.0	53.73	18.02	.908	55.63	56.92	738.83	
1200.0	50.14	16.06	.912	51.31	52.39	653.39	
1250.0	45.53	13.96	.914	46.03	46.88	561.22	
1300.0	39.70	11.70	.910	39.61	40.23	462.23	
1350.0	32.41	9.31	.893	31.87	32.28	357.11	
1400.0	23.44	6.87	.840	22.62	22.85	248.86	
1450.0	12.69	4.63	.656	11.74	11.85	149.39	
1500.0	.00	3.72	.112	.00	.00	.00	

Fig. 3: Analytical calculated electromagnetic torque, electrical stator and rotor current as well as power factor versus speed.

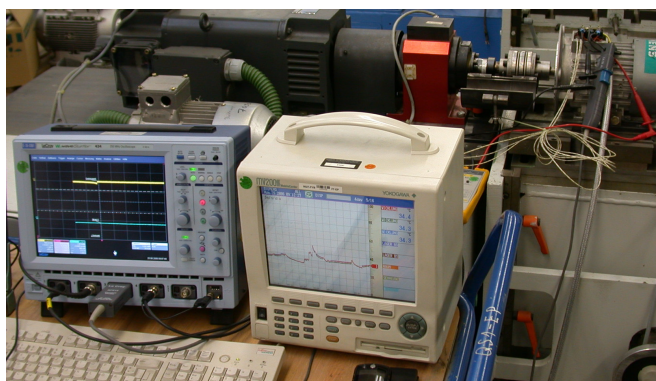


Fig. 4: Measurement set-up of the machine to be investigated on the test rig.

The usage of more complex and much accurate concepts, such as the coupled transient electromagnetic-mechanical finite element calculation method with directly coupled external circuits is very useful, because it allows a deeper and more detailed insight into various secondary effects. Thus, e.g. current and torque ripple, local magnetic saturation effects in distinct lamination parts, origin of additional losses and influence of movement to higher harmonics can be studied very extensively and therefore become more visible during the design phase [2,3,4].

In order to verify the calculated results for the transient as well as quasi-steady operational states, extended measurements have been performed with the test-set up shown in Fig. 4.

II. FINITE ELEMENT MODELING

Within the 2D modeling, several assumptions have to be made in order to describe the physical motor of Fig. 1 in a realistic manner. Moreover, the used iron stator and rotor laminations, as shown in Fig. 5 and Fig. 6 are magnetically non-linear. Thus, time-discretization and linearization methods are necessary in order to solve these kinds of coupled electromechanical problems [1,2,5].

A good correlation between the numerical calculated and the measured quantities also strongly depend on the chosen values of the input parameters. Erroneous measurement will slightly increase this undesired natural gap.

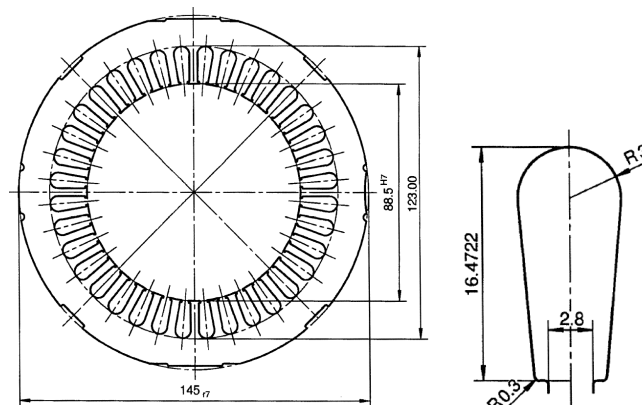


Fig. 5: Stator lamination with 36 slots (left) and details of one single slot (right) with according dimensions. The stator has a single layer winding system embedded inside the slots.

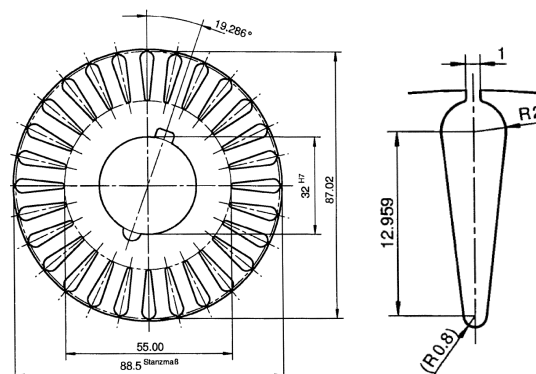


Fig. 6: Rotor lamination with 28 slots (left) and details of one single slot (right) with according dimensions. The rotor has a aluminum casting squirrel-cage.

The input values of copper and aluminum materials are very sensitive to changing thermal conditions but that effect is not directly covered within the used electromechanical Finite Element approach. However, such effects are indirectly regarded due to the variation of resistance parameters [6,9,10].

A. Electromagnetic field and electric circuit coupling in the time-domain

The local field quantities of the two-dimensional Finite Element algorithm must be coupled to electric circuits, as shown in Fig. 7, in order to include external parameters representing the end-regions of the machine. The activated voltage supply network can thereby be arbitrarily dependent on time [1,2,5].

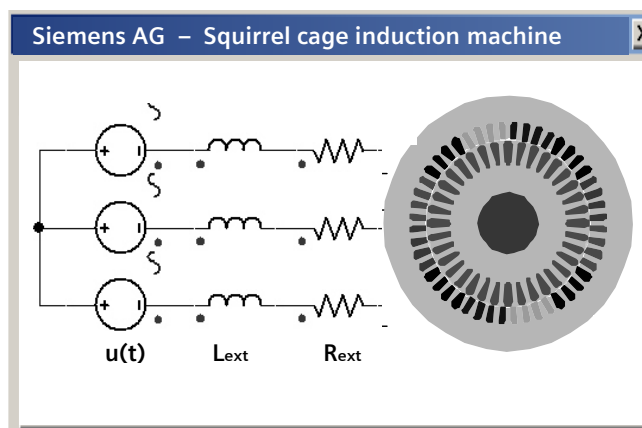


Fig. 7: Schematically structure for the direct coupling of external circuits to the Finite Element model of the squirrel cage machine with rotating rotor part in the time-domain.

B. Modeling with symmetry usage

The machine symmetry allows for modeling only one quarter of the machine. Fig. 8 shows the cross section of the machine used within the finite element calculation [1,2].

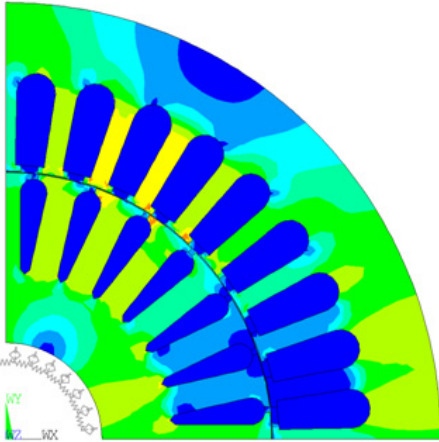


Fig. 8: Plot of the magnetic flux density for a distinct time-step at the rated operational state .

C. Inclusion of end winding effects

The ohmic part of the stator end-winding is indirectly taken into consideration by a decreasing conductivity value. The value of the conductivity depends on the winding temperature. This is valid for both the stator winding and the rotor winding. Within the model, those parameters are adapted in relation to the winding temperatures in the operational state [9,10,11].

The short circuit ring of the squirrel cage winding is modeled by means of concentrated electrical resistances between two adjacent damper bars of each ring segment. The leakage inductance of the end rings are taken into consideration as additional values at the end leakage inductance of the stator winding. The end leakage inductance is in generally given with

$$L_s = \frac{4\pi^2}{10} \cdot \left(\frac{z_1}{100}\right)^2 \cdot \frac{1}{100} \cdot \frac{1}{2p} \cdot \lambda_s \cdot \frac{l_{s,1}}{1} , \quad (1)$$

whereby λ_s is the end leakage conductance and $l_{s,1}$ the length of the end winding. Within the start up behavior of the machine, the value in (1) is constant and will not change due to saturation [6,7,8].

D. Influence of skewed rotor bars

Skewing of the damper bars in the rotor is normally omitted within the 2D modeling. The effects of the missing skewing of the rotor bars on the magnetic 2D circuit of the machine can be roughly approximated with

$$f_{\text{skew}} = \frac{\sin \frac{\beta}{2}}{\frac{\beta}{2}} \gg 1 - 0.41 \left(\frac{2p}{n_s}\right)^2 \approx 1 - 0.41 \left(\frac{4}{36}\right)^2 = 0.005 \quad (2)$$

which means that the influence of skewing is almost small in quasi-steady operational state, whereas some inaccuracies are occurring during the transient state [6,7,8,9,11].

Unfortunately, the effect of omitting the skewing (2) becomes visible within the Fast Fourier transformation of the time-dependent torque. The obtained ripple of the 2D calculation contains too many harmonic components, which are in reality omitted due to 3D skewing. However, an averaging procedure of the calculated 2D torque courses by subdividing the spatially displaced torque according to the skewing angle and finally added delivers an adequate substituted 3D torque value.

III. LOCAL FIELD QUANTITIES AT THE NOMINAL QUASI-STEADY OPERATIONAL STATE

The application of the transient Finite Element procedure with applied sinusoidal time-dependent source voltages in Fig. 7 allows a very close look into the local distribution of the electromagnetic flux density inside the airgap when the quasi-steady operational state of the machine is reached. Moreover, associated time-dependent electrical currents at the terminals in Fig. 7 are obtained [1,2].

A. Radial air gap flux density component

The radial component of the magnetic flux density along the special circumferential airgap distance is shown in Fig. 9 for the nominal working point.

For the plotted fundamental wave in Fig. 9 the amplitude is 0.83 T. The machine is only modeled in the 2-D therefore the slot ripples can be seen clearly. The harmonic number caused by the stator slots is given by

$$v_s = c_1 \cdot \frac{n_s}{p} + 1 \cdot \quad (3)$$

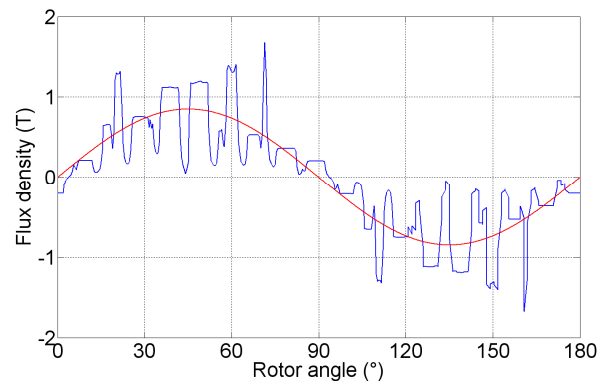


Fig. 9: Magnetic flux density (blue line) with fundamental wave (red line).

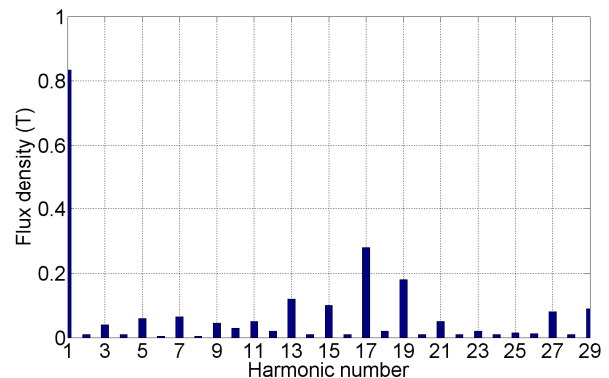


Fig. 10: FFT of the air gap flux density at rated load.

In (3), the coefficient c_1 is a positive and negative integer without zero and n_s is the integer number of 36 stator slots. The equation for the rotor is analogous to (3) established by

$$v_R = c_1 \cdot \frac{n_R}{P} + 1 \tag{4}$$

with n_R of 28 rotor slots. For the fundamental wave of the stator currents the harmonic numbers caused by the stator slots are -17, +19, -35, +37 and so on. The harmonic numbers -13, +15, -27, +29, etc. are caused by the rotor slots. These harmonics also become visible in the FFT of the air gap field from Fig. 9, which is shown in Fig. 10.

As a result in a three-phase-winding system, only odd harmonic numbers in the spectrum, see Fig.6, like -5, +7, -11, +13 etc. are obvious. Harmonic numbers of 3, 6, 9, etc. are not visible in the air gap flux density of a three phase machine.

B. Time-dependency of the line-to-line current

The invoked higher stator current frequencies of the time-courses due to slotting are calculated with

$$f_s = \gamma \cdot \frac{n_R}{P} \cdot (1 - s) \pm 1, \tag{5}$$

where n_R is the number of rotor slots, s the slip and γ a positive integer with zero. The lowest harmonic number in (5) leads to the frequencies 612.6 Hz and 712.6 Hz. From Fig. 11 it is evident, that, except from the fundamental frequency, these two frequencies have an important role in the stator current spectrum. Other frequencies in Fig. 11 with the harmonic order 3 are caused by the saturation of the magnetic circuit.

C. Time-dependency of the rotor bar current

The calculated time-dependent rotor current is shown in Fig. 12 for the nominal working point. The analysis of the calculated time-dependent current paths in the frequency domain leads to the frequencies given in Table 1. Thereby, the fundamental wave with 2.6 Hz is clearly visible.

The higher harmonic current components are plotted in Fig. 13. The frequency value 50 Hz has always the harmonic number one. The frequencies around 280 Hz correlate with the 5th and 6th harmonic number and the frequencies around 570 Hz correlate with the 11th harmonic number. The distinct component at the frequency around 850 Hz is associated to the 17th harmonic number and is mainly caused by the stator slots.

TABLE 1
FREQUENCIES OF THE ROTOR BAR CURRENTS

Harmonic number	Value	Unit
1	2.6	Hz
-5	286.6	Hz
+7	281.3	Hz
-11	570.6	Hz
+13	565.3	Hz
-17	854.6	Hz
+19	849.3	Hz

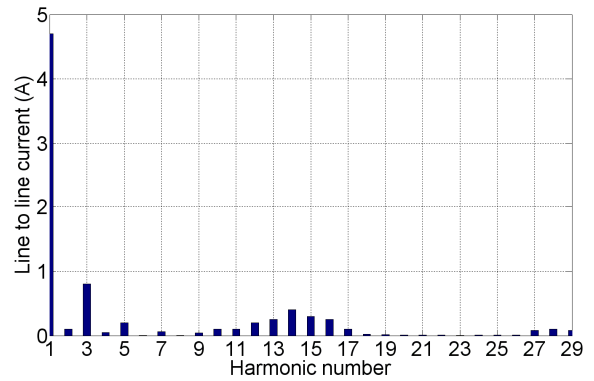


Fig. 11: FFT of the line-to-line current at the nominal working point.

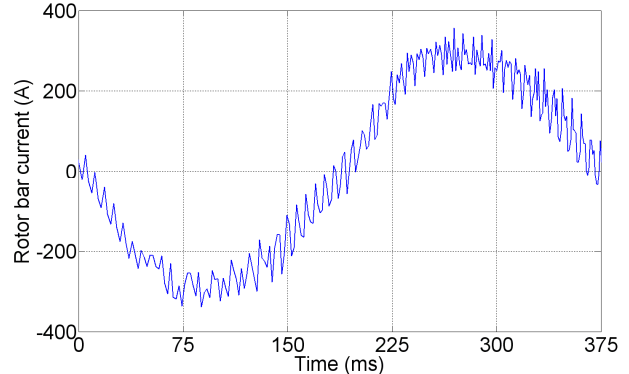


Fig. 12: Numerical calculated current of one rotor bar at the rated speed of 1420 rpm.

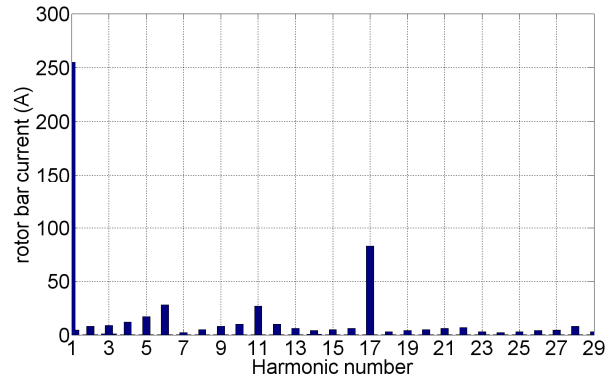


Fig. 13: FFT of rotor bar current at nominal working point.

D. Invoked electromagnetic torque

The torque of electromagnetic origin is numerically calculated with the virtual work principle, whereby some difficulties arising with the Maxwell stress tensor method are omitted [1,2].

The time-dependent torque curve at the nominal point is shown in Fig. 14. The mean value of the torque is about 19.72 Nm. The according frequencies of the harmonic torque components, often called torque ripple, can be calculated because of the known harmonic rotor current frequencies. On the base of the rotor bar currents, the frequencies of the torque are given as

$$f_t = (-1) \cdot f_1 \cdot s \cdot |1 - v \cdot (1 - s)| \tag{6}$$

for the frequencies caused by positive rotating magneto motive forces [6,8,9].

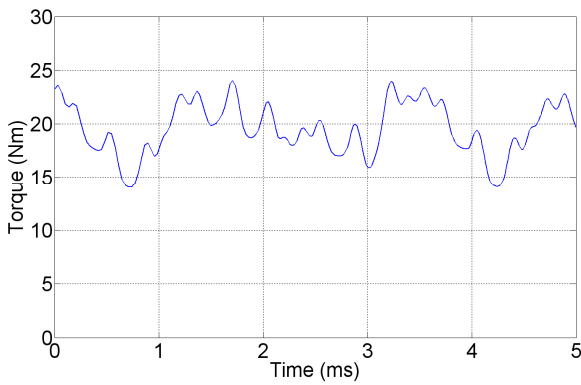


Fig. 14: Numerical calculated time-dependent electromagnetic torque at the nominal working point.

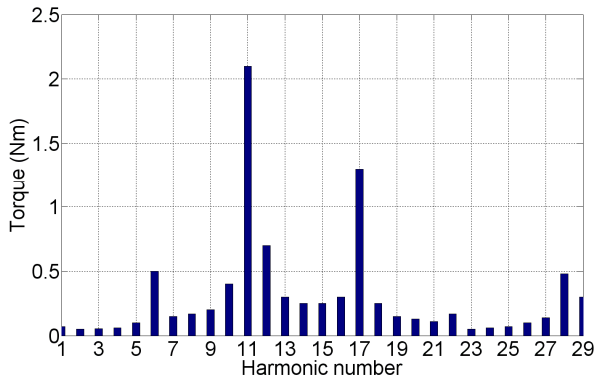


Fig. 15: FFT of the torque ripple at the nominal working point.

Those evoked by the negative rotating magneto motive forces are given with

$$f_t = f_1 \cdot s \cdot |1 - \nu \cdot (1 - s)|. \quad (7)$$

The most important frequencies from (6) and (7) are summarized in Table 2. However, only the not shown frequency contribution of 0 Hz produces the constant torque of the motor [6,8,9].

Due to the restrictions concerning the skewing of the rotor bars within the applied 2D finite element model it is obviously clear that a lot of frequencies in Fig. 15 are therefore considerably increased.

However, the actually amounts of the rotor winding system can be retroactive estimated by the winding factor given by

TABLE 2
FREQUENCIES OF THE TORQUE RIPPLE

Harmonic number	Value	Unit
1	2.6	Hz
-5	289.3	Hz
+7	278.6	Hz
-11	573.3	Hz
+13	562.6	Hz
-17	857.3	Hz
+19	846.6	Hz

TABLE 3
WINDING FACTORS OF THE ROTOR WINDING

Harmonic number	Value	Unit
1	0.9916	1
-5	0.8	1
+7	0.64	1
-11	0.25	1
+13	0.076	1
-17	-0.163	1
+19	-0.211	1

$$\xi_{r,\nu} = \frac{\sin\left(\nu \cdot \frac{\varepsilon}{\tau_p} \cdot \frac{\pi}{2}\right)}{\nu \cdot \frac{\varepsilon}{\tau_p} \cdot \frac{\pi}{2}}. \quad (8)$$

Table 3 shows that the amplitudes of the higher harmonic numbers due to slotting are decreasing. If the winding factor (8) is considered, the torque ripple reduces up to 2% at the nominal point.

IV. QUASI-STEADY STATE ANALYSIS

Typically quasi-steady characteristics of the squirrel cage induction machine have been automatically obtained by processing calculated numerical results, which are obtained from the solver for applied time-dependent voltages in Fig. 7 and certain speed values. Thus a direct comparison of those numerical calculated results with basic test results is straightforward. Additionally, further comparisons to listed results in Fig. 3 received from well suited analytical calculation methods are possible [1,2,6].

A. Quasi-steady speed-torque characteristic

The Fig. 16 shows the calculated and measured speed-torque-characteristic of the machine. The calculated data corresponds very well to the measured curve. The difference that happens can be explained by a slightly higher temperature level of the machine compared to the assumed temperature.

B. Electrical line-to-line current

The line-to-line current is the sum of two phase currents due to delta connection. The curve in Fig. 17 shows the electrical line-to-line current as a function of the motor speed. It should be mentioned that only the fundamental wave of the current, obtained from the FFT of the calculated time-dependent course, is presented in Fig. 17.

C. Power factor

To be able to define the phase shift with sufficient accuracy, a relative small time-step is applied to solve the nonlinear problem. The Fig. 18 shows the measured and calculated power factor. For the nominal working point, the power factor is calculated as 0.84, whereas the one given by the measurement is 0.8.

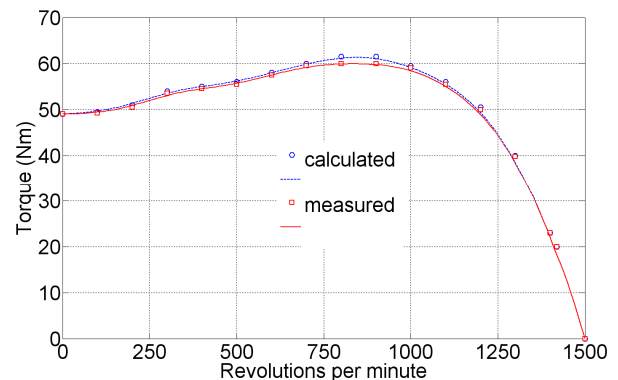


Fig. 16: Numerical calculated (blue line) and measured (red line) speed-torque characteristic.

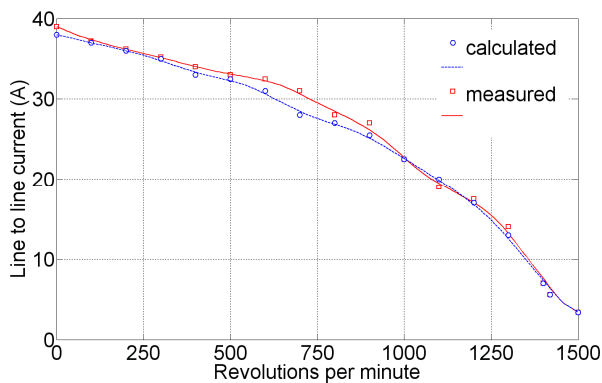


Fig. 17: Numerical calculated (blue line) and measured (red line) line-to-line current of the delta connected machine versus speed.

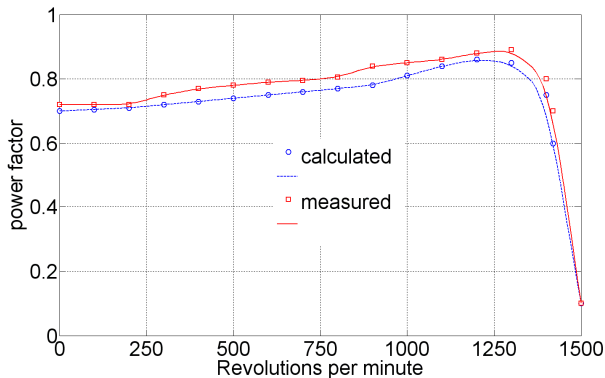


Fig. 18: Numerical calculated (blue line) and measured (red line) power factor versus speed.

V. TRANSIENT START-UP ANALYSIS

The full transient behavior of electromechanically quantities, such as e.g. current, speed and torque, of the machine from standstill under load or no-load is numerically calculated for a default sinusoidal time-dependent voltage in Fig. 7 with the time-stepping method. Especially during the start up of an induction motor the significant influence of the end windings on the transient behavior has to be considered. Additionally, the effects of the absent skew of the rotor bars in a 2-D finite element model are analyzed [1,2,6,7,8].

A. Time-dependency of the speed

Without any load, the calculated machine reaches the nominal speed within less than one turnaround. This explains the high dynamical overshoot in Fig. 19. The motor speed is additionally measured by a tachometer. Undeterminable variation of friction behavior as well as ventilating losses during the start-up is also responsible for the difference between measured and calculated curves in Fig. 19.

B. Invoked electromagnetic torque

The Fig. 20 shows the calculated torque characteristics of the induction machine in dependency on time. Due to the very low threshold frequency of the torque shaft it was not possible to measure the torque during the startup.

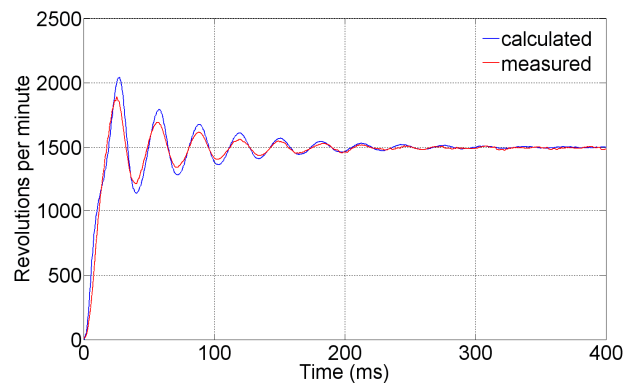


Fig. 19: Numerical calculated (blue line) and measured (red line) speed characteristics versus time.

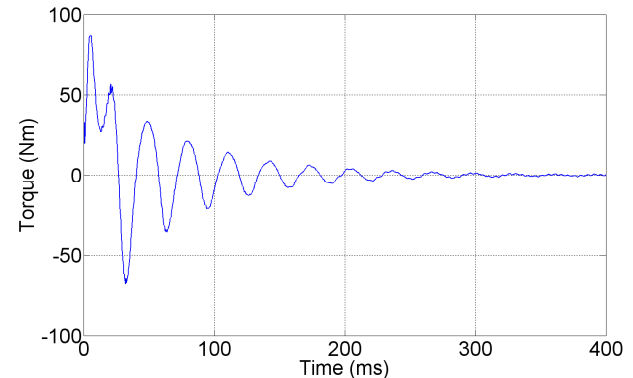


Fig. 20: Numerical calculated electromagnetic torque characteristics versus time.

C. Time-dependency of the electrical current

The numerically calculated line-to-line current of the machine during the start up is shown in Fig. 21. There is a quite good correspondence between the measured and calculated value. Differences between the two curves are caused by slightly different switching on-times, but not by the saturation effects of the end leakage reactance of the machine. This is evident because of the big geometrical distance between the stator end windings and the laminated sheet package.

D. Time-dependency of the rotor bar current

Fig. 22 shows the derived plot in the rotor bar during the startup of the unloaded machine, whereas the very high inrush peaks during the acceleration are obvious.

E. Dynamic speed-torque characteristic

The torque characteristic during the starting of an induction motor can be divided into four parts. The maximum torque is given by

$$T_{\text{Max}} \approx T_{\text{Start}} \cdot \left(1 + \frac{1}{\cos \varphi_{\text{Start}}} \right), \quad (9)$$

where $\cos \varphi_{\text{Start}}$ represents the short circuit power factor. The maximum torque of induction machines is usually substantial greater than the starting torque. Fig. 23 shows additionally the calculated speed-torque characteristic at no-load.

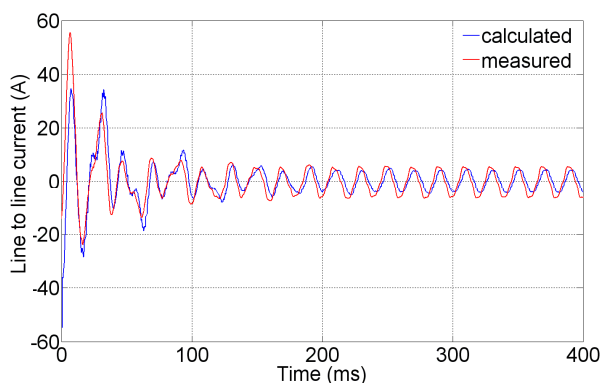


Fig. 21: Numerical calculated (blue line) and measured (red line) line-to-line current of the delta connected machine during the transient start-up case.

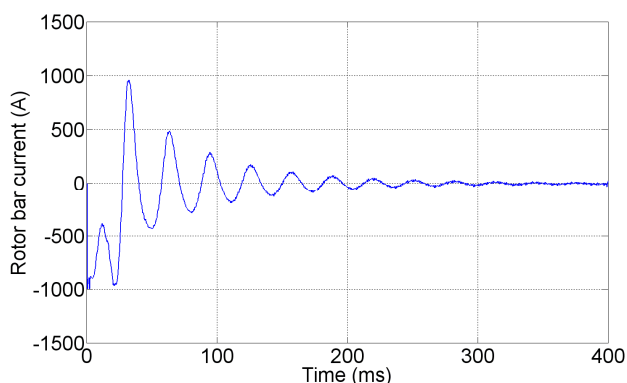


Fig. 22: Numerical calculated single rotor bar current course during the start-up.

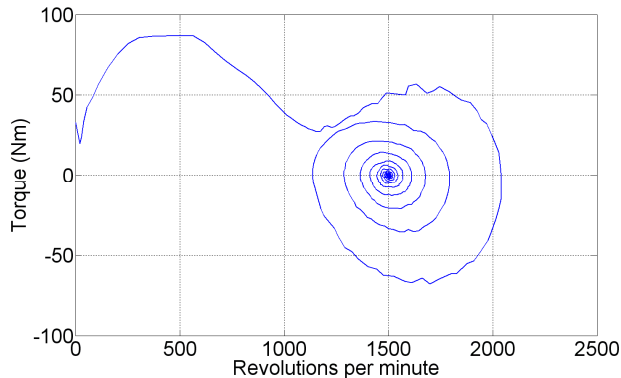


Fig. 23: Reproduced speed-torque characteristic of the unloaded machine from numerical results.

VI. CONCLUSION

A two-dimensional transient electromagnetic-mechanical finite element calculation, which fully takes account of non-linear and time-dependent motional effects, has been applied to the time-domain analysis of a squirrel cage induction motor.

Fortunately, the finite element algorithm is directly coupled to external network circuits in order to take account of additional motor parameters due to three-dimensional effects. Thus, quasi-steady and full transient characteristics could be predicted straightforward with high accuracy. A good agreement between numerically calculated and measured quantities could be achieved.

REFERENCES

- [1] Salon J.S.: *Finite element analysis of electrical machines*. Cambridge: Cambridge University Press, 1996.
- [2] Bastos J.P.A., Sadowski N.: *Electromagnetic modeling by finite element methods*. New York: Marcel Dekker Inc., 2003.
- [3] Binns K.J., Lawrenson P.L., Trowbridge C.W.: *The analytical and numerical solution of electric and magnetic fields*. Chichester: John Wiley and Sons Ltd., 1992.
- [4] Davat B., Ren Z., Lajoic-Mazenc M.: *The movement in field modeling*. IEEE Transactions on Magnetics, Vol.21, No.6, 1985.
- [5] Kohnke P.: *Theory reference released version 6.1*. Ansys Inc., Canonsburg, USA, April 2002.
- [6] Bödefeld Th., Sequenz H.: *Elektrische Maschinen, Eine Einführung in die Grundlagen*. Wien New York: Springer-Verlag, 1971.
- [7] Kovács K.P.: *Transiente Vorgänge in Wechselstrommaschinen*, Band 1. Budapest: Verlag der Ungarischen Akademie der Wissenschaften, 1959.
- [8] Kovács K.P.: *Transiente Vorgänge in Wechselstrommaschinen*, Band 2. Budapest: Verlag der Ungarischen Akademie der Wissenschaften, 1959.
- [9] Königshofer T.: *Die Wicklungen elektrischer Maschinen*. Berlin: Technischer Verlag Herbert Cram, 1969.
- [10] Königshofer T.: *Die praktische Berechnung elektrischer Maschinen*. Berlin: Technischer Verlag Herbert Cram, 1959.
- [11] Sequenz H.: *Wicklungen elektrischer Maschinen*. Wien New York: Springer Verlag, 1954.



J. Bacher received the MSc and PhD degree in Electrical Engineering from the Graz University of Technology in 1998 and 2002, respectively. Since 2002 he is senior scientist at the Institute of Drive Technology and Electrical Machines at the Graz University of Technology, where his research studies are covering all types of electrical machines and transformers.



C. Grabner received the MSc from the Vienna University of Technology in 1999 and the PhD degree from the Graz University of Technology in 2002. Afterward he joined the Automation and Drives division of Siemens AG in Germany. As a principal scientist within the Research and Development Department he is responsible for the development of innovative drive systems focusing on power converter topologies, software architectures as well as electrical motor designs. Mr. Grabner is a member of the International Electrotechnical Commission (IEC) as well as the Germany Commission for Electro-technic (DKE).